FRONTIER LETTER

CrossMark

Source rupture processes of the foreshock and mainshock in the 2016 Kumamoto earthquake sequence estimated from the kinematic waveform inversion of strong motion data

Kimiyuki Asano[*] and Tomotaka Iwata

Abstract

The 2016 Kumamoto earthquake sequence started with an M_{JMA} 6.5 foreshock occurring along the northern part of the Hinagu fault, central Kyushu, Japan, and the M_{JMA} 7.3 mainshock occurred just 28 h after the foreshock. We analyzed the source rupture processes of the foreshock and mainshock by using the kinematic waveform inversion technique on strong motion data. The foreshock was characterized by right-lateral strike-slip occurring on a nearly vertical fault plane along the northern part of the Hinagu fault, and it had two large-slip areas: one near the hypocenter and another at a shallow depth. The rupture of the mainshock started from the deep portion of a northwest-dipping fault plane along the northern part of the Hinagu fault, then continued to transfer to the Futagawa fault. Most of the significant slip occurred on the Futagawa fault, and the shallow portion of the Hinagu fault also had a relatively large slip. The slip amount on the shallowest subfaults along the Futagawa fault was approximately 1–4 m, which is consistent with the emergence of surface breaks associated with this earthquake. Right-lateral strike-slip dominated on the fault segment along the Hinagu fault, but normal-slip components were estimated to make a significant contribution on the fault segment along the Futagawa fault. The large fault-parallel displacements recorded at two near-fault strong motion stations coincided with the spatiotemporal pattern of the fault slip history during the mainshock. The spatial relationship between the rupture areas of the foreshock and mainshock implies a complex fault structure in this region.

Keywords: 2016 Kumamoto earthquake, Source rupture process, Kinematic source inversion, Strong motion data, Futagawa and Hinagu faults

Introduction

The 2016 Kumamoto earthquake sequence started with an M_{JMA} 6.5 earthquake at a shallow depth in Kumamoto Prefecture, which is in the central part of Kyushu Island, southwest Japan, at 21:26 Japan Standard Time (JST) on April 14, 2016 (12:26 UTC on April 14, 2016). A larger earthquake of M_{JMA} 7.3 occurred at 01:25 JST on April 16, 2016 (16:25 UTC on April 15, 2016), just 28 h after

the M_{JMA} 6.5 earthquake (Fig. 1). Hereafter, we call the M_{JMA} 6.5 event of April 14 the "foreshock" and the M_{JMA} 7.3 event on April 16 the "mainshock." Moment tensor solutions determined routinely by NIED (Fukuyama et al. 1998) and the Global CMT Project (Ekström et al. 2012) are also shown in Fig. 1b. Both events generated severe strong ground motions in the near-source region, and the ground motion during the mainshock was felt in most of southwest Japan. A seismic intensity observation station at Mashiki town hall (93051, red triangle in Fig. 1a) recorded a seismic intensity of 7 on the Japan Meteorological Agency (JMA) scale during both events,

*Correspondence: k-asano@egmdpri01.dpri.kyoto-u.ac.jp
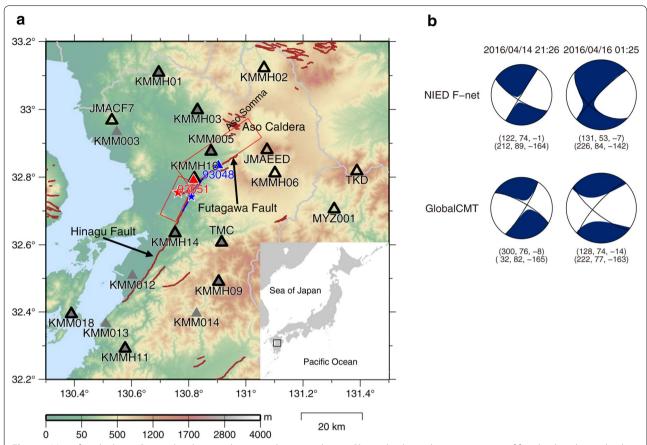Disaster Prevention Research Institute, Kyoto University, Gokasho, Uji, Kyoto 611-0011, Japan

Fig. 1 **a** Map of studied area. *Rectangle* in lower-right inset indicates study area. *Blue* and *red stars* denote epicenters of foreshock and mainshock, respectively. *Blue* and *red rectangles* represent surface projection of assumed source fault planes of foreshock and mainshock, respectively. *Triangles* indicate strong motion stations used. Stations used for source inversion analysis of foreshock are *gray-filled*, and stations used for source inversion analysis of mainshock are bordered by *thick lines*. *Brown lines* represent surface traces of active faults compiled by Nakata and Imaizumi (2002). **b** Moment tensor solutions of foreshock and mainshock determined by F-net of NIED (Fukuyama et al. 1998) and Global CMT Project (Ekström et al. 2012)

and another station at Nishihara village hall (93048, blue triangle in Fig. 1a) recorded a seismic intensity of 7 during the mainshock. These two near-fault stations belong to the seismic intensity information network deployed by the Kumamoto prefectural government, and their observed records were released via the JMA.

This earthquake sequence occurred along the Futagawa fault zone and the northern part of the Hinagu fault zone in central Kyushu. The Futagawa–Hinagu fault system is one of the major active fault systems on Kyushu Island and is a right-lateral strike-slip fault system. This fault system is thought to be part of the western extension of the Median Tectonic Line, which is the longest active right-lateral strike-slip fault in Japan (e.g., Chida 1992; Okada 1980; Yeats 2012). The average horizontal slip rate of the Futagawa–Hinagu fault system has been 0.88 mm/year in the late Quaternary (Tsutsumi and Okada 1996). Surface breaks caused by

the mainshock were found along the Futagawa–Hinagu fault system by emergency field surveys (e.g., Geological Survey of Japan 2016; Okada and Toda 2016). The crustal deformation and surface rupture along the Futagawa–Hinagu fault system were also identified by multiple-aperture interferometry (MAI) analysis using ALOS-2/PALSAR-2 data (Yarai et al. 2016). These observational results imply that the fault rupture is associated with the Futagawa fault and northern part of the Hinagu fault.

This paper focuses on the source rupture processes of the two significant events during the 2016 Kumamoto earthquake sequence based on kinematic waveform inversion analyses using strong motion data. The obtained spatiotemporal source models were compared with reported surface breaks, displacement time histories observed at near-fault strong motion stations, and the seismic activity during this earthquake sequence.

Methods

The kinematic source rupture processes of the two earthquakes were estimated with the multiple time-window linear waveform inversion method (Hartzell and Heaton 1983; Olson and Apsel 1982). This method is commonly used to infer the kinematic source rupture process of large inland crustal earthquakes (e.g., Asano et al. 2005; Ma et al. 2001; Sekiguchi et al. 2000; Tanaka et al. 2014; Wald and Heaton 1994; Yoshida et al. 1996). The observational equation is based on the representation theorem (Maruyama 1963; Burridge and Knopoff 1964) and was discretized in space and time. For discretization in space, the assumed fault plane was divided into small subfaults. For discretization in time, the temporal moment release history at the center of each subfault was represented by several time windows, and its basis function was a smoothed ramp function. The optimum number of time windows was determined by trial and error during a preliminary analysis. The unknown model parameters were the amplitude of the basis functions corresponding to each time window at each subfault. The rupture front of the first time window propagated radially at a constant velocity from the rupture starting point, which was fixed at the hypocenter determined by JMA. The rake angle variation was limited within a certain range, as described in Table 1. In order to suppress excessive complexity, we included a spatiotemporal smoothing constraint following Sekiguchi et al. (2000). The relative weight of the smoothing constraint equation against the observational equation was determined to minimize Akaike's Bayesian information criterion (ABIC) (Akaike 1980). The inverse problem was solved using the linear least-squares method with a nonnegative constraint (Lawson and Hanson 1974).

We assumed a single nearly vertical fault plane for the M_{JMA} 6.5 foreshock based on its aftershock distribution and the moment tensor solution by the F-net project of the National Research Institute for Earth Science and Disaster Resilience (NIED, Fukuyama et al. 1998). The strike and dip angles of the fault plane were 212° and 89°, respectively. For the M_{JMA} 7.3 mainshock, we assumed a fault model consisting of two fault segments based on the aftershock distribution and the surface trace of known active faults. Figure 2 shows spatial distributions of the foreshocks and aftershocks in four periods. The aftershock distribution after the mainshock implies that the fault planes of the mainshock dipped northwestward, whereas the aftershocks of the foreshock occurring before the mainshock appeared to align vertically. The first segment (segment #1) was set along the Hinagu fault, and the second (segment #2) was set along the Futagawa fault. The difference in strike angles between the two segments was 30°. We assumed that the rupture propagated smoothly from the Hinagu fault to the Futagawa fault with no time lag. Spatiotemporal smoothing was applied to each fault segment separately. Table 1 summarizes the detailed information on the settings of the waveform inversion analyses.

We used strong ground motion data observed by K-NET, KiK-net, and F-net, which are nationwide observation networks operated by NIED (Okada et al. 2004; Aoi et al. 2011), and strong motion data from the JMA seismic intensity observation network (Nishimae 2004). Records from downhole sensors were used for the KiK-net

Table 1 Summary of settings in waveform inversion analysis

	Foreshock	Mainshock	
Origin time[a]	2016/04/14 21:26:34.43	2016/04/16 01:25:05.47	
Epicenter[a]	32.7417°N, 130.8087°E	32.7545°N, 130.7630°E	
Hypocenter depth[a]	11.39 km	12.45 km	
Fault segment		#1	#2
Strike/dip	212°/89°	205°/72°	235°/65°
Rake angle variation	−164° ± 45°	−142° ± 45°	−142° ± 45°
Length	14 km	14 km	28 km
Width	13 km	18 km	18 km
Subfault size	1 km × 1 km	2 km × 2 km	
Number of subfaults	182	63	126
Number of time windows	5	9	
Duration/time-shift of time window	1.0 s/0.5 s	1.0 s/0.5 s	
Target frequency range	0.05–1 Hz	0.05–0.5 Hz	
Resampling of data	10 Hz	5 Hz	
Number of stations	13	15	

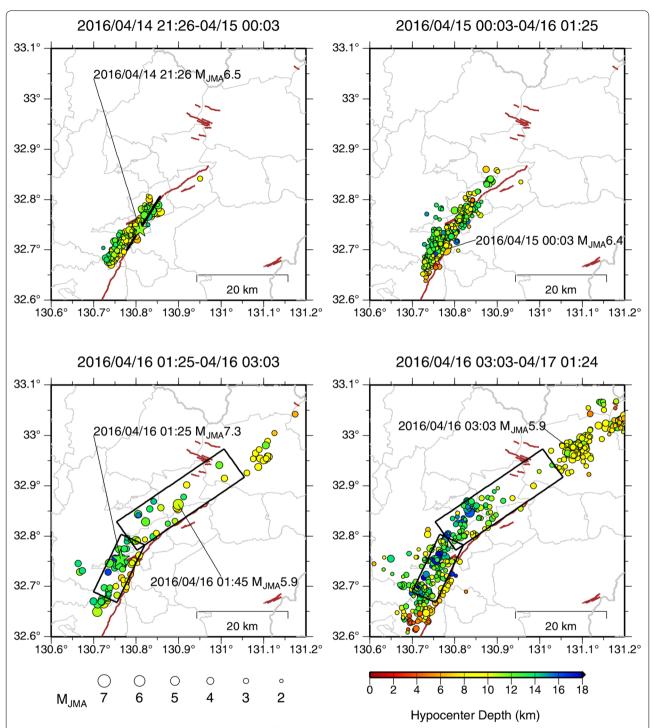[a] Origin time and hypocenter were taken from the JMA unified earthquake catalog

Fig. 2 Aftershocks larger than JMA magnitude of 2 in four different periods and fault models. *Size* and *color of circles* correspond to magnitude and depth of aftershocks. *Rectangles* represent surface projection of assumed source fault planes of foreshock and mainshock in inversion analyses

stations. K-NET and JMA have sensors at the ground surface, and F-net sensors are installed in a vault. Original acceleration data were numerically integrated into velocity in the time domain except at the F-net stations, which had a velocity-type strong motion seismograph installed. The S-wave portion of three-component velocity waveforms was used in the analysis. Figure 1 shows a map of the strong motion stations used in the analyses.

Theoretical Green's functions were calculated using the discrete wavenumber method (Bouchon 1981) with the reflection and transmission matrix method (Kennett and Kerry 1979). A one-dimensional velocity structure model was assumed for each station, considering the depth at which the sensor was installed. Because sedimentary layers over the seismic bedrock affect the amplitude and shape of seismic waveforms, considering the difference in velocity structure models among strong motion stations is quite important to preparing reliable Green's functions (e.g., Asano and Iwata 2009). Thus, a different one-dimensional velocity structure model was prepared for each station (Fig. 3); these were extracted from the three-dimensional Japan Integrated Velocity Structure Model (Koketsu et al. 2012). The smallest S-wave velocity in this velocity structure model was 350 m/s. Both the data and Green's functions were bandpass-filtered prior to the inversion analysis.
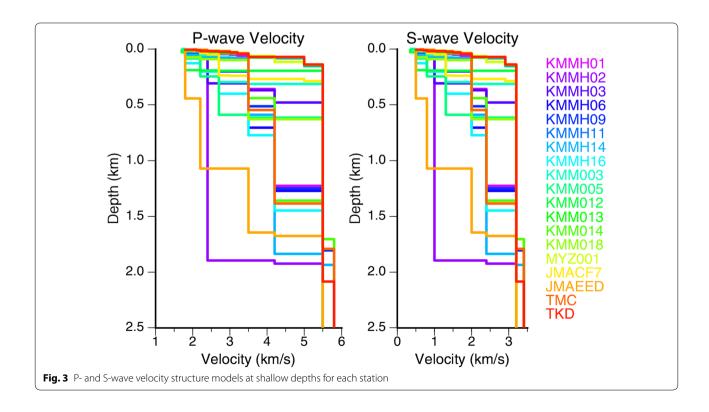
Results and discussion

Source rupture process of foreshock

Figure 4a shows the resulting final slip distribution of the foreshock. The obtained source model had a seismic moment of 2.04×10^{18} N-m (M_W 6.1). The maximum and average slips were 1.16 and 0.36 m, respectively. The best estimate for the propagation velocity of the first time-window triggering front was 2.2 km/s. The variance reduction was 37.7 %.

The duration of moment release was approximately 2 s at most subfaults (Fig. 4b), and the total duration of the rupture was approximately 8 s (Fig. 4c). Right-lateral strike-slip dominated the rupture area. A large slip was found near the hypocenter or rupture starting point. The rupture mainly propagated upward and northeastward (Fig. 4c), and another large-slip area ruptured approximately 4 s after the origin time at a depth of 5 km, close to the northeastern end of the Hinagu fault beneath the town of Mashiki, where a seismic intensity of 7 was recorded. The rupture propagation toward the southwest was not significant during this foreshock. Instead, another M_{JMA} 6.4 earthquake occurred at 00:03 JST on April 15, 2016, about 2.5 h after the foreshock at a depth of 6.71 km, close to the southwestern end of the foreshock's rupture area (see the top-right panel in Fig. 2). The synthetic waveforms reproduced the observed waveforms well (Fig. 4d).

Source rupture process of mainshock

Significant slip occurred along the Futagawa fault (segment #2), as shown by the resulting final slip distribution of the mainshock in Fig. 5a. The obtained source model had a seismic moment of 4.50×10^{19} N-m (M_W 7.0), which was 22 times larger than the foreshock. The maximum and average slips were 5.13 and 1.87 m, respectively. The best estimate for the propagation velocity of the first time-window triggering front was 2.4 km/s.
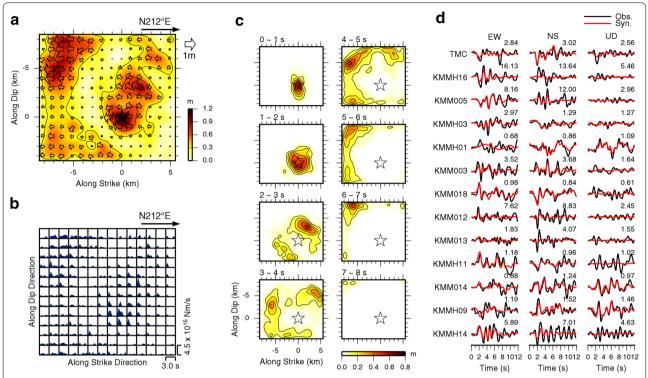

Fig. 3 P- and S-wave velocity structure models at shallow depths for each station

Fig. 4 Source model of foreshock. **a** Spatial distribution of final slips on fault plane with contour interval of 0.3 m. *Arrow* shows slip vector of hanging wall relative to foot wall. *Open star* indicates hypocenter or rupture starting point. **b** Obtained moment-rate function for each subfault. **c** *Snapshot* of temporal slip progression every 1 s. **d** Comparison of observed velocity waveforms (*black traces*) and synthetic velocity waveforms (*red traces*). Velocity waveforms were bandpass-filtered from 0.05 to 1 Hz. Waveform amplitudes were normalized by the maximum observed amplitude. Maximum observed amplitude of each component is shown above each trace in centimeters per second. *EW* east–west, *NS* north–south, *UD* up–down

With this source model, the synthetic waveforms reproduced the characteristics of the observed waveforms well (Fig. 5c). The variance reduction was 45.3 %.

The large slip in fault segment #1 was concentrated at a shallow depth at the northeastern end of the Hinagu fault, where surface breaks were also reported by emergency field surveys (e.g., Geological Survey of Japan 2016; Okada and Toda 2016). The rupture of segment #2 started at the deep portion of the fault and extended upward and northeastward; it ceased to rupture within 20 s (Fig. 6). The duration of moment release was longer in shallow subfaults than in deeper subfaults (Fig. 5b). The slip amount of the shallowest subfaults along the Futagawa fault was approximately 1–4 m, which is consistent with the emergence of surface breaks associated with this earthquake (e.g., Geological Survey of Japan 2016; Okada and Toda 2016). The slip direction on segment #1 was close to pure right-lateral strike-slip, and that on segment #2 had a significant normal-slip component, particularly in the large-slip area. The northeastern end of the rupture area of the mainshock was located inside the Aso caldera. However, it was previously thought before this

earthquake sequence that the Futagawa fault system lay to the west of the Aso somma, and did not extend to the caldera. Although most of the large-slip area was along the previously known Futagawa fault outside the Aso somma, non-negligible slips were estimated to be inside the western part of the Aso caldera, where surface breaks generated by this mainshock were also discovered (e.g., Geological Survey of Japan 2016). Thus, it could be that the Futagawa fault system extends to the Aso caldera and is concealed by thick volcanic deposits within the caldera.

As stated in the Introduction, the acceleration time histories on the ground surface were recorded at two near-fault stations. The locations of these two stations (93048 at Nishihara village hall and 93051 at Mashiki town hall) are indicated in the snapshots in Fig. 6 and the map in Fig. 1. These two stations were located within 2 km of the surface trace of the Futagawa fault. Thus, the fault-parallel motion at these stations can be considered to resemble the nearby fault motion. We calculated the displacement waveforms from the observed acceleration records by double integration in the time domain with the appropriate baseline correction but did not perform any filtering
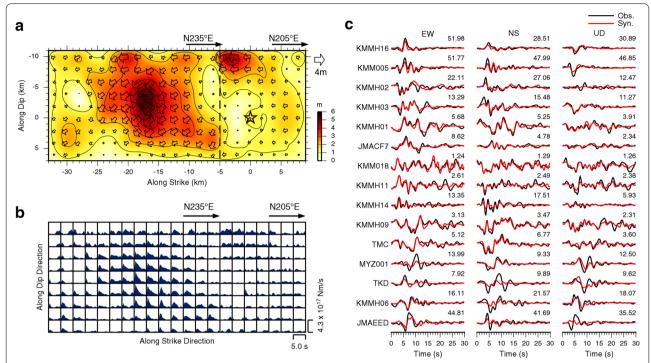
Fig. 5 Source model of mainshock. **a** Spatial distribution of final slips on fault plane with contour interval of 1.0 m. *Arrow* shows slip vector of hanging wall relative to foot wall. *Open star* indicates hypocenter or rupture starting point. *Dashed lines* represent boundaries of fault segments #1 and #2. **b** Obtained moment-rate function for each subfault. **c** Comparison of observed velocity waveforms (*black traces*) and synthetic velocity waveforms (*red traces*). Velocity waveforms were bandpass-filtered from 0.05 to 0.5 Hz. Waveform amplitudes were normalized by the maximum observed amplitude. Maximum observed amplitude of each component is shown above each trace in centimeters per second. *EW* east–west, *NS* north–south, *UD* up–down

of these data. Figure 6 shows the comparison of the particle motions on the horizontal plane obtained from these displacement waveforms with the rupture snapshots for each timeframe. Because the timing and amount of the fault-parallel displacements coincided with the spatiotemporal slip history estimated by the kinematic waveform inversion of the strong motion data, we confirmed that the obtained source model represents the spatiotemporal slip history during this event.

Figure 7 shows the comparison of waveforms by forward modeling for these two near-fault stations. Both the velocity and displacement waveforms are shown in this figure. These near-fault stations are located on a ground surface covered with Quaternary terrace deposits and volcanic deposits (e.g., Hoshizumi et al. 2004), so precise modeling of a shallow velocity structure is necessary to recover the amplitude at these stations. For station 93051, the permanent displacement in the NS and UD components was explained well by this model, but the EW component was not perfectly reproduced. The permanent displacements in the EW and UD components for station 93,048 were also underestimated. Because the permanent displacement or near-field term in such near-fault

ground motions is generally sensitive to the locations and minute geometry of causative faults and attenuates rapidly with distance (e.g., Hisada and Bielak 2003), more detailed modeling of surface breaking faults at shallow depths is necessary to improve ground motion modeling in near-fault areas. Fault discretization is also crucial for near-fault ground motion modeling. Nevertheless, the synthetic velocity and displacement waveforms explained the phases in the observed waveforms well.

Spatial relationships among foreshock, mainshock, and aftershocks

The final slip distributions for the foreshock and mainshock were compared with the spatial distributions of the aftershocks. Figure 8a shows a map view of the final slip distribution of the mainshock with aftershocks ($M_{JMA} > 2$) occurring within 24 h of the mainshock. On fault segment #1 along the Hinagu fault, the large-slip area at shallow depth had a small number of aftershocks. Fault segment #2 had a relatively small number of aftershocks during this period, particularly in the northeastern half of the fault plane located inside the Aso caldera. There was an area with seismic activity north of Mt. Aso
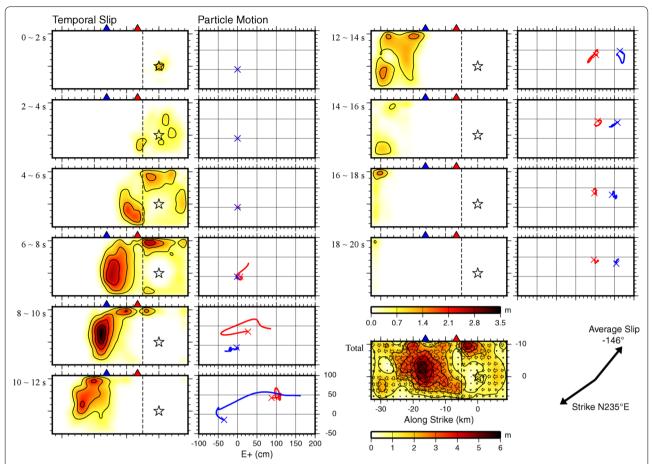
Fig. 6 Temporal slip progression during mainshock and observed displacements at near-fault stations. *Left panel* of each *row* shows *snapshot* of temporal slip progression every 2 s. *Right panel* shows horizontal particle motions on ground surface corresponding to each timeframe at two near-fault stations. *Red* Mashiki town hall (station #93051, *red triangle* in *left panel*); *blue* Nishihara village hall (station #93049, *blue triangle* in *left panel*); *cross* location at beginning of timeframe

(Fig. 8a) that was outside the rupture area of the mainshock. We think that this seismic activity was remotely triggered by the change in regional stress due to the mainshock.

The large slip of the foreshock and small events immediately after this foreshock also seem to have had a complementary distribution in space (Fig. 8b). Although the fault plane of the foreshock was partially overlain with that of the mainshock, the exact locations of large slips at shallow depth were not the same as those of the mainshock.

Fault segment #1 of the mainshock spatially overlapped the rupture area of the foreshock but had a different dip angle from the fault plane of the foreshock. That is, the rupture of the mainshock was initiated on another fault plane closely parallel to the fault plane of the foreshock along the Hinagu fault, as expected from the difference in spatial patterns of the hypocenters before and after

the mainshock (Fig. 2), and continued to be transferred to the Futagawa fault. This implies a complex fault structure along the Futagawa–Hinagu fault system. In order to examine this hypothesis, further studies on aftershock relocation and reflection surveys to image the complex structure of fault planes in the source region are necessary.

The M_W 7.9 Denali earthquake on November 3, 2002, was an inland crustal earthquake along the Denali fault system, Alaska, and was preceded by the M_W 6.7 Nenana Mountain earthquake on October 23, 2002. The aftershocks of the Nenana Mountain earthquake formed a vertical plane along the Denali fault system. The rupture of the Denali earthquake started on the Susitna Glacier fault, which is a splay fault south of the McKinley strand of the Denali fault system, where the Nenana Mountain earthquake occurred. It then propagated eastward along the main strand of the Denali fault system. (e.g.,
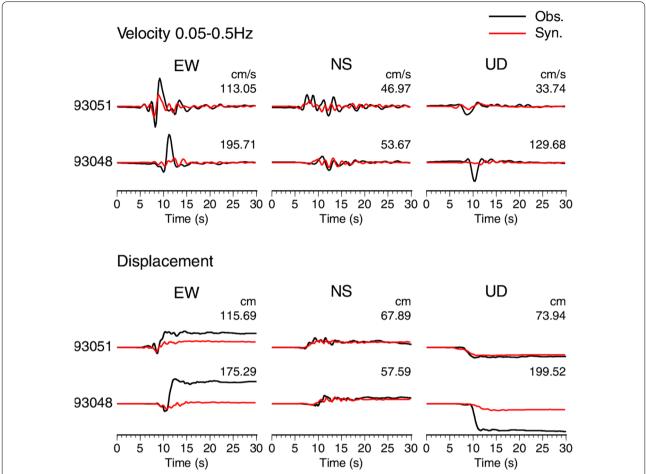
Fig. 7 Waveform comparison by forward modeling for two near-fault stations. (*top*) Comparison of observed velocity waveforms (*black traces*) and synthetic velocity waveforms (*red traces*). Velocity waveforms were bandpass-filtered from 0.05 to 0.5 Hz. Waveform amplitudes were normalized by the maximum observed amplitude. Maximum observed amplitude of each component is shown above each trace in centimeters per second. (*bottom*) Comparison of observed displacement waveforms (*black traces*) and synthetic displacement waveforms (*red traces*). *EW* east–west, *NS* north–south, *UD* up–down

Ratchkovski et al. 2004). The spatial and temporal relationships between the foreshock and mainshock of the 2016 Kumamoto earthquake sequence look similar to those of the 2002 Denali earthquake sequence.

Conclusions

The source rupture processes of the foreshock and mainshock in the 2016 Kumamoto earthquake sequence were estimated by kinematic waveform inversion of strong motion data. The foreshock was a right-lateral strike-slip event occurring on a nearly vertical fault plane along the northern part of the Hinagu fault, and two large-slip areas were found near the hypocenter and at shallow depth. The rupture of the mainshock started from the deep portion of a northwest-dipping fault plane along the Hinagu fault. Then, it continued to be transferred to the Futagawa fault and propagated northeastward and upward to generate significant slips with surface breaks. The peak slip of the mainshock was 5.1 m, including the normal component of the slip, and the duration of the rupture was approximately 20 s. The slip amount of the shallowest subfaults along the Futagawa fault was approximately 1–4 m, which is in rough agreement with the emergence of surface breaks associated with the mainshock. The large fault-parallel displacements at two near-fault stations coincided with the spatiotemporal pattern of the fault slip history during the mainshock. The spatial relationship between the rupture areas of the foreshock and mainshock implies a complex fault structure in this region. The central and southern parts of the Hinagu fault were not ruptured during this earthquake sequence.
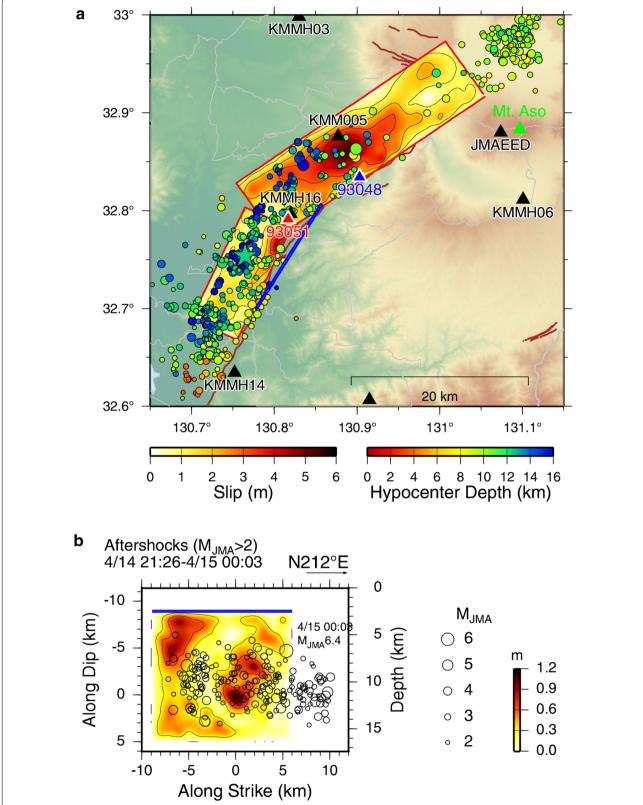
Fig. 8 Comparison between spatial slip distributions and aftershocks. **a** Map view of final slip distribution on fault plane of mainshock, with aftershocks within 24 h after mainshock. *Blue line* represents surface projection of source fault plane of foreshock. **b** Comparison of final slip distribution of foreshock with aftershocks occurring from 21:26 JST on April 14, 2016, to 00:03 JST on April 15, 2016

References
Akaike H (1980) Likelihood and the Bayes procedure. Trab Estad Invest Oper 31:143–166

Aoi S, Kunugi T, Nakamura H, Fujiwara H (2011) Deployment of new strong motion seismographs of K-NET and KiK-net. In: Akkar S, Gülkan P, van Eck T (eds) Earthquake data in engineering seismology. Geotechnical, geological, and earthquake engineering, vol 14. Springer, Dordrecht, pp 167–186

Asano K, Iwata T (2009) Source rupture process of the 2004 Chuetsu, Mid-Niigata prefecture, Japan, earthquake inferred from waveform inversion with dense strong-motion data. Bull Seismol Soc Am 99:123–140

Asano K, Iwata T, Irikura K (2005) Estimation of source rupture process and strong ground motion simulation of the 2002 Denali, Alaska, earthquake. Bull Seismol Soc Am 95:1701–1715

Bouchon M (1981) A simple method to calculate Green's function for elastic layered media. Bull Seismol Soc Am 71:959–971

Burridge R, Knopoff L (1964) Body force equivalents for seismic dislocations. Bull Seismol Soc Am 54:1875–1888

Chida N (1992) Active faults in Central Kyushu, Southwest Japan—Quaternary faulting along the Median Tectonic Line in Kyushu. Mem Geol Soc Jpn 40:39–51 **(in Japanese with English abstract)**

Ekström G, Nettles M, Dziewonski AM (2012) The Global CMT Project 2004–2010: Centroid-moment tensors for 13,017 earthquakes. Phys Earth Planet Inter 200–201:1–9

Fukuyama E, Ishida M, Dreger DS, Kawai H (1998) Automated seismic moment tensor determination by using on-line broadband seismic waveforms. J Seismol Soc Jpn 51:149–156 **(in Japanese with English abstract)**

Geological Survey of Japan, AIST (2016) 2016 Kumamoto earthquakes: report 4. GSJ Chishitsu News 5:169–174 **(in Japanese)**

Hartzell SH, Heaton T (1983) Inversion of strong ground motion and teleseismic waveform data for the fault rupture history of the 1979 Imperial Valley, California, earthquake. Bull Seismol Soc Am 73:1553–1583

Hisada Y, Bielak J (2003) A theoretical method for computing near-fault ground motions in layered half-spaces considering static offset due to surface faulting, with a physical interpretation of fling step and rupture directivity. Bull Seismol Soc Am 93:1154–1168

Hoshizumi H, Ozaki M, Miyazaki K, Matsuura H, Toshimitsu S, Uto K, Utsumi S, Komazawa M, Hiroshima T, Sudo S (2004) Geological Map of Japan 1:200,000, Kumamoto, Geological Survey of Japan, AIST

Kennett BLN, Kerry NJ (1979) Seismic waves in a stratified half space. Geophys J R Astron Soc 57:557–583

Koketsu K, Miyake H, Suzuki H (2012) Japan integrated velocity structure model version 1. In: Proceedings of the 15th world conference on earthquake engineering, Lisbon, 24–28 September 2012

Lawson CL, Hanson RJ (1974) Solving least squares problems. Prentice-Hall, Old Tappan

Ma K-F, Mori J, Lee S-J, Yu SB (2001) Spatial and temporal distribution of slip for the 1999 Chi-Chi, Taiwan, earthquake. Bull Seismol Soc Am 91:1069–1087

Maruyama T (1963) On the force equivalents of dynamic elastic dislocations with reference to the earthquake mechanism. Bull Earthq Res Inst Univ Tokyo 41:467–486

Nakata T, Imaizumi T (eds) (2002) Digital active fault map of Japan. University of Tokyo Press, Tokyo

Nishimae Y (2004) Observation of seismic intensity and strong ground motion by Japan Meteorological Agency and local governments in Japan. J Jpn Assoc Earthq Eng 4(3):75–78

Okada A (1980) Quaternary faulting along the Median Tectonic Line of southwest Japan. Mem Geol Soc Jpn 18:79–108

Okada S, Toda S (2016) Report on the emergency field survey of the 2016 Kumamoto earthquake. Report presented at the second emergency meeting, International Research Institute of Disaster Science, Tohoku University, Sendai, 19 April 2016. http://irides.tohoku.ac.jp/media/files/earthquake/eq/IRIDeS_Kumamoto_earthquake_okada_20160419.pdf. Accessed 16 May 2016

Okada Y, Kasahara K, Hori S, Obara K, Sekiguchi S, Fujiwara H, Yamamoto A (2004) Recent progress of seismic observation networks in Japan Hi-net, F-net, K-NET and KiK-net. Earth Planets Space 56:xv–xxviii. doi:10.1186/BF03353076

Olson AH, Apsel RJ (1982) Finite faults and inverse theory with applications to the 1979 Imperial Valley earthquake. Bull Seismol Soc Am 72:1969–2001

Ratchkovski NA, Wiemer S, Hansen RA (2004) Seismotectonics of the Central Denali fault, Alaska, and the 2002 Denali fault earthquake sequence. Bull Seismol Soc Am 94:S156–S174

Sekiguchi H, Irikura K, Iwata T (2000) Fault geometry at the rupture termination of the 1995 Hyogo-ken Nanbu earthquake. Bull Seismol Soc Am 90:117–133

Tanaka M, Asano K, Iwata T, Kubo H (2014) Source rupture process of the 2011 Fukushima-ken Hamadori earthquake: how did the two subparallel faults rupture? Earth Planets Space 66:101. doi:10.1186/1880-5981-66-101

Tsutsumi H, Okada A (1996) Segmentation and Holocene surface faulting on the Median Tectonic Line, southwest Japan. J Geophys Res 101:5855–5871

Wald DJ, Heaton TH (1994) Spatial and temporal distribution of slip for the 1992 Landers, California, earthquake. Bull Seismol Soc Am 84:668–691

Wessel P, Smith WHF (1998) New, improved version of generic mapping tools released. EOS Trans Am Geophys Union 79:579

Yarai H, Kobayashi T, Morishita Y (2016) Crustal deformation around the faults revealed by MAI analysis. http://www.gsi.go.jp/cais/topic160428-index-e.html. Accessed 8 May 2016

Yeats R (2012) Active faults of the world. Cambridge University Press, New York

Yoshida S, Koketsu K, Shibazaki B, Sagiya T, Kato T, Yoshida Y (1996) Joint inversion of near- and far-field waveforms and geodetic data for the rupture process of the 1995 Kobe earthquake. J Phys Earth 44:437–454